View metadata, citation and similar papers at core.ac.uk

brought to you by CORE

provided by Purdue E-Pubs

Purdue University
Purdue e-Pubs

International Refrigeration and Air Conditioning Conference

School of Mechanical Engineering

2018

Defrosting Performance of Patterned Heat Transfer Surfaces with a Superhydrophobic Silica Nanosprings Coating

Nickolas C. Schmiesing
Miami University, Oxford, OH, United States of America, schmienc@miamioh.edu

Griffin Barrington
Miami University, United States of America, barringt@miamioh.edu

Giancarlo Corti
Miami University, United States of America, corticlg@miamioh.edu

Andrew Sommers
Dept. of Mechanical and Manufacturing Engineering, Miami University, Oxford, OH 45056, sommerad@miamioh.edu

Follow this and additional works at: https://docs.lib.purdue.edu/iracc

Schmiesing, Nickolas C.; Barrington, Griffin; Corti, Giancarlo; and Sommers, Andrew, "Defrosting Performance of Patterned Heat Transfer Surfaces with a Superhydrophobic Silica Nanosprings Coating" (2018). *International Refrigeration and Air Conditioning Conference*. Paper 1897.
https://docs.lib.purdue.edu/iracc/1897

This document has been made available through Purdue e-Pubs, a service of the Purdue University Libraries. Please contact epubs@purdue.edu for additional information.
Complete proceedings may be acquired in print and on CD-ROM directly from the Ray W. Herrick Laboratories at https://engineering.purdue.edu/Herrick/Events/orderlit.html

Defrosting Performance of Patterned Heat Transfer Surfaces with a Superhydrophobic Silica Nanosprings Coating

Nickolas C. SCHMIESING[1], Griffin T. BARRINGTON[1], Giancarlo CORTI[1,*], Andrew D. SOMMERS[1,*]

[1] Dept. of Mechanical and Manufacturing Engineering, Miami University, Oxford, OH 45056 USA
Phone: (513) 529-0718, Fax: (513) 529-0717, E-mail: corticlg@miamioh.edu, sommerad@miamioh.edu

* Corresponding Author

ABSTRACT

The overall aim of this work was to study the defrosting performance of functionalized heat transfer surfaces containing a novel, silica nanosprings coating combined with preferential microstructural roughness. In doing this, differences in drainage rates and defrosting effectiveness were explored both on patterned and non-patterned surfaces. To date, ten different surfaces have been examined— an uncoated, untreated aluminum plate (S1), plates containing a silica nanospring (SN) coating of varying thickness (S2-S6), a plate containing evenly-spaced microchannels both with and without the SN surface coating (S7, S8), and then finally a plate containing a microstructural roughness gradient both with and without the SN surface coating (S9, S10). Cyclical tests containing both frosting and defrosting periods were conducted on each sample. For these experiments, the frost layer was grown inside a controlled environmental test chamber where the relative humidity (RH) was held constant (i.e. 60%, 80%) while the temperature of the ambient air inside the enclosure was monitored to ensure consistency. The surface temperature of the plate was fixed using a thermoelectric cooler (TEC) typically at -8°C, -10°C or -12°C. The TEC unit was placed on an electronic balance within the test chamber, which permitted the frost mass to be recorded continuously during testing.

Overall, the defrosting effectiveness varied from 56-96% across all the surfaces depending on the test conditions. For the tests performed at 60% RH, the uncoated baseline surfaces tended to have defrosting efficiencies in the range of 59-75%, while the nanospring-coated surfaces tended to have defrosting efficiencies in the range of 66-96%. Different nanospring mat thicknesses were also explored as part of this work, which showed that an optimum thickness likely exists with shorter overall mat thicknesses being preferred. The microstructural surface gradient pattern included in this work was designed to create "preferential lanes" on the surface for drainage. The surface which yielded the highest overall defrosting efficiency during testing was the surface with the uniformly-spaced microchannels and nanospring coating (S8), while the gradient surface design with nanospring coating (S10) also generally performed well versus the baseline surface, especially at lower plate temperatures (i.e. T_w = -10 and -12°C).

1. INTRODUCTION

The study of frost formation and the defrosting of surfaces remain important when designing new frost-tolerant heat exchangers and systems. Because frost growth blocks the flow of air through the heat exchanger, lower air-side heat transfer rates (stemming from the porous structure of the frost layer and its low overall thermal conductivity) and higher air-side pressure drops are generally realized. As a result, refrigerator evaporators generally require periodic defrosting to help curb these performance losses. Unfortunately, this periodic defrosting requirement is inherently inefficient due the associated downtime. Over the years, different techniques (i.e. hot gas bypass, recirculation frost control, etc.) have been used for performing the defrost, and different design strategies have been employed to try and mitigate the problem (i.e. fin staging, spine fins, increased fin pitch, etc.). Fin surface wettability modification has also been studied; however, relatively few papers could be found which have specifically examined the influence of wettability on a surface's defrosting performance. Thus, the development and study of new frost-tolerant surfaces represent an important issue for the HVAC&R industry, and additional research is needed.

Numerous frost studies and frost growth models have been published. For example, O'Neal and Tree (1984), Padki et al. (1989), and Iragorry et al. (2004) have each performed a critical review of the literature and tried to summarize the effect that various environmental parameters have on frost properties and frost growth models. Other early works focused on the measurement and prediction of frost properties on conventional surfaces include Yonko and Sepsy

(1967), Hayashi et al. (1977), Tokura et al. (1983), Tao et al. (1993), and Lee et al. (1997). Later works include Cheng and Cheng (2001), Yun et al. (2002), and Kandula (2011), Yang and Lee (2004), El Cheikh and Jacobi (2014), and Hermes et al. (2014). In Hermes et al. (2014), a new semi-empirical model for predicting the time-dependent porosity and density of a frost layer was presented as a function of the modified Jakob number. It is worth noting that this model (which was derived initially from first-principles) is independent of the frost surface temperature, using the plate surface temperature instead.

Papers concerned with the influence of surface wettability on the frosting/defrosting behavior of surfaces were generally harder to find. In Rahimi (2015), incipient ice formation was studied on aluminum surfaces with different chemical modifications (i.e., PEG and PFOS) and nano-roughness. It was found that at the initial stage of ice formation, flat hydrophobic surfaces exhibit the lowest ice formation rate, the smallest thickness, and the highest ice density. Faster ice formation and lower ice density on the untreated aluminum was attributed to the highly heterogeneous nature of the bare aluminum surface, leading to a broad distribution of surface energies on the microscopic and the formation of low-density feather-like ice structures. In another study, Kulinich et al. (2011) showed that super-hydrophobic surfaces are also not always ice-repellent and that the ice-repellent properties of super-hydrophobic materials can deteriorate during icing/deicing cycles due to damage to the surface asperities. They also showed that the anti-icing efficiency of super-hydrophobic surfaces is significantly lower in a humid atmosphere due to increased ice adhesion strength. In Liu and Kulacki (2018), defrost experiments were performed on superhydrophilic, baseline, and superhydrophobic aluminum plates. On the superhydrophobic surface, "frost slumping" was observed in which the frost layer falls off as a rigid body. On the superhydrophilic and baseline surfaces, the frost layer maintains contact with the surface, but as it melts may partially fall off with the draining meltwater. Their results showed that the "frost slumping" phenomenon generally shortens the defrost time and improves defrosting efficiency. A recent review of the literature by Song and Dang (2018) highlights the various methods used in the measurement of frost properties, including different mathematical models and correlations.

In a paper by Shin et al. (2003), frost formation characteristics were studied on flat hydrophilic surfaces having advancing dynamic contact angles (DCA) of 23°, 55°, and 88° in a wind tunnel. They found that during the initial frost growth period, the shape of the micro droplets on the surface depended upon the surface energy, and the process of frost crystal growth was affected by the advancing contact angle. High DCA surfaces showed the presence of irregular and rough crystals during the initial period of frost deposition, which resulted in high frost thickness and low frost density, whereas low DCA surfaces tended to produce low frost thickness and high frost density. Hoke et al. (2004) examined surfaces that were both hydrophilic and hydrophobic and discussed the effect of surface wettability and its impact on condensate distribution (the initial condition for frost growth). Interestingly, recent papers such as Liu et al. (2008), Wang et al. (2015), Fang and Amirfazli (2014), and Cai et al. (2011) have all shown that super-hydrophobic surfaces may be able to restrain frost growth on the surface due to the high energy barrier for frost crystal nucleation on these surfaces. Delayed frosting times of as long as 55-60 minutes have been reported. This delay has been attributed to the underlying nanostructure of super-hydrophobic surfaces, which traps air pockets near the surface which in turn exhibits an insulating behavior and results in a decrease in droplet surface contact area (Tourkine et al., 2009). In a related work by Huang et al. (2012), the effect of the contact angle on the water droplet freezing process was studied. Their results show that the contact angle has a direct influence on both the water droplet freezing time and frost crystal growth velocity. A review of surface manufacturing methods and frost formation characteristics on hydrophobic and superhydrophobic surfaces was recently performed by Kim et al. (2017).

Other recent works concerned with droplet coalescence, freezing, and/or defrosting on engineered and coated surfaces include Boreyko et al. (2013, 2016), Van Dyke et al. (2015), and Schmiesing and Sommers (2017). Several recent works were also found published by Kim and Lee. In Kim and Lee (2011), the influence of the fin surface static contact angle (i.e. SCA = 2.5°, 75°, and 142°) on the frosting/defrosting performance of a heat pump under winter operating conditions was studied. On the hydrophobic surface, frost retardation was observed but the effect was not very significant. The degree of required super-cooling however for the onset of frost nucleation was affected by the hydrophobic surface treatment. In comparison, the frost layer on the hydrophilic fin was thinner and had a greater average density. Overall, the effect of surface contact angle on the defrosting time was found to be insignificant. In Kim and Lee (2012), the impact of surface treatment on the air-side pressure drop of surface-treated, louvered-fin heat exchangers was examined. More specifically, a hydrophilic louvered fin (SCA = 3°), hydrophobic louvered fin (SCA = 130°), and a dual-coated fin were investigated. The hydrophilic heat exchanger had the highest air-side pressure drop under frost conditions but the lowest under wet-conditions. In a follow-up work (Kim and Lee, 2013), the influence of the fin pitch (i.e. 14-18 FPI) on the frosting/defrosting behavior of the surface-treated, louvered-fin heat

exchangers was studied. The ratio of retained water (following the defrost) was the highest on the hydrophobic coil, but this coil also showed the highest overall heat transfer rate during repeated frosting/defrosting experiments due to frost retardation and no noticeable leading edge effect at T_r = –9.5°C and T_a = 3°C. As the refrigerant temperature was decreased however to –12°C, the effect of frost retardation was weakened.

In summary, although it is well-known that surface wettability can affect condensate retention on a heat exchanger and the properties of a growing frost layer, very few papers were found in the open literature which specifically address the influence of surface wettability on defrosting behavior and defrosting effectiveness. Moreover, the range of applicability for those papers is often quite limiting. In addition, metrics for comparing the defrosting performance of surfaces over different defrosting times and conditions were generally found to be lacking aside from the routine reporting of defrosting percentage with one exception (Schmiesing and Sommers, 2017). This highlights the need for additional study on the defrosting performance of surfaces. In this work, differences in drainage rates and defrosting behavior were explored on silica nanosprings (SN) coated surfaces (both patterned and non-patterned) with an emphasis placed on assessing performance variations over multiple frosting/defrosting cycles and comparing performance with other surfaces.

2. EXPERIMENTAL METHOD

2.1 Test Surfaces / Silica Nanosprings

In this study, frosting/defrosting experiments were performed with the purpose of assessing the defrosting performance of the surface and issues related to multiple frost/defrost events. During these tests, the surface temperature was prescribed using a thermoelectric cooler (TEC). The air temperature and relative humidity were also recorded during each test and held constant using cool mist ultrasonic humidification. Each test lasted three hours and thirty minutes and consisted of three one-hour frost growth periods each followed by a ten minute defrosting period (i.e. three cycles). The test samples were constructed from aluminum alloy 5052 polished on one side to a brushed finish. The test surfaces all had the same dimensions and were approximately 99.5 mm × 80.2 mm × 3.4 mm in size. Details about the various plates and their differences in surface structure can be found in Table 1.

All of the surfaces (except Surface 1) were coated with silica nanosprings (SN) (see Fig. 1). Silica nanosprings are a unique high-surface-area, one-dimensional nanomaterial made of amorphous silica (Wang et al., 2006). SN offer several advantages over other one-dimensional nanostructures such as: mild growth conditions at 350°C and atmospheric pressure (Wang et al., 2006), thermally stable >1000°C in air, innate hydrophilicity, more than 350m^2/g of accessible surface area (Corti et al., 2013) and photolithography compatible (Sai et al., 2011; Timalsina et al., 2010). The silica nanosprings grow via a modified vapor-liquid-solid (VLS) mechanism is discussed in detail elsewhere in the literature (Wang et al., 2006). The atmospheric processes allow growth of a 60 μm mat of SN in less than 30 min. Over the past few years, the application area has grown from less than a centimeter square to more than 400cm^2 with growth rates of ~2.5 μm/min, which translates to approximately 350mg/h. Another unique advantage, SN can

Table 1: Matrix of heat transfer test surfaces

No.	Material	Gradient?	Surface Features	Growth Period	Surface ID
S1	Al	No	Baseline Surface	--	--
S2	Al	No	Baseline Surface + SN Coating Thickness 1	30 min	SN30
S3	Al	No	Baseline Surface + SN Coating Thickness 2	15 min	SN15
S4	Al	No	Baseline Surface + SN Coating Thickness 3	5 min	SN5
S5	Al	No	Baseline Surface + SN Coating Thickness 4	2 min	SN2
S6	Al	No	Baseline Surface + SN Coating Thickness 5	1 min	SN1
S7	Al	No	Uniform Channels (No Coating)	--	--
S8	Al	No	Uniform Channels + SN Coating Thickness 4	--	--
S9	Al	**Yes**	Gradient Surface (No Coating)	--	--
S10	Al	**Yes**	Gradient Surface + SN Coating Thickness 4	--	--

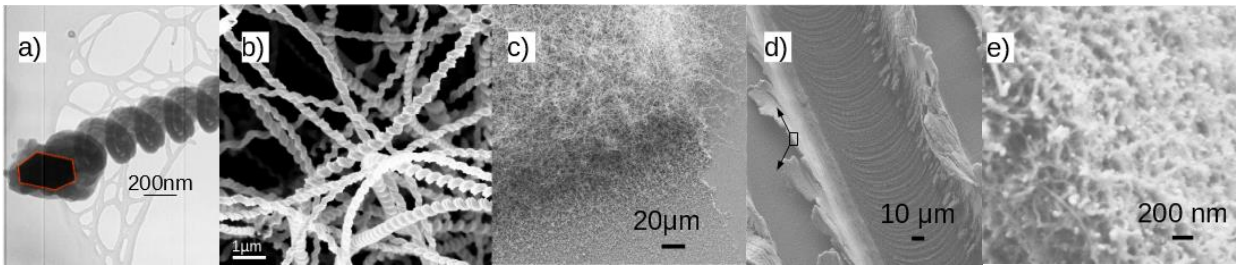

Figure 1: Silica nanosprings— (a) Au nanoparticle at the tip of a SN; (b) silica nanosprings; (c) glass slide coated with a patterned SN; (d) a 25µm groove coated with a thin layer of SN and (e) detail of the 25µm groove wall.

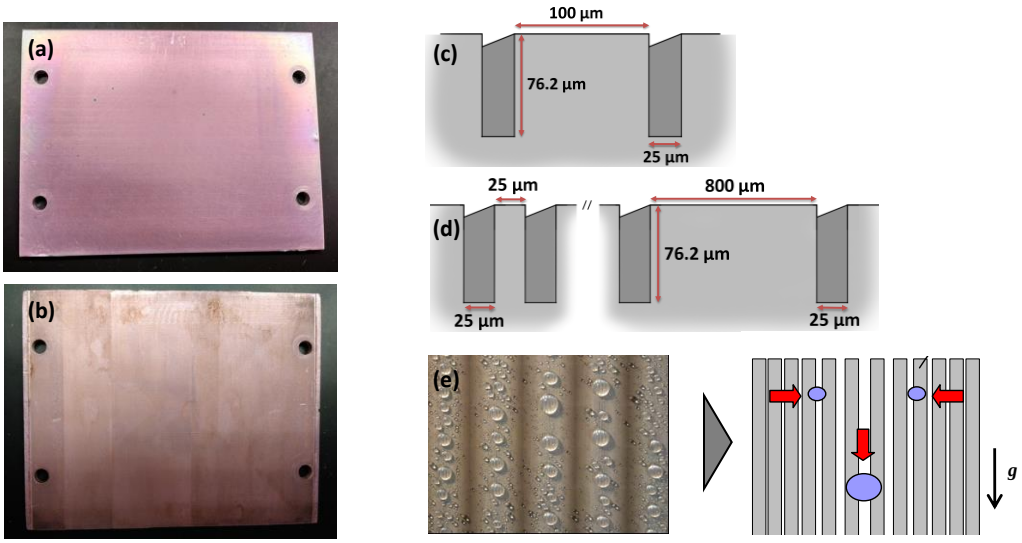

Figure 2: Pictures of some of the test plates: (a) Surface 5, (b) Surface 8, (c) uniform channels (Surfaces 7-8), (d) gradient geometry (Surfaces 9-10), and (e) motivating idea based on a spray test on a laser-etched surface.

conformably coat most substrates (2-D and 3-D) that can withstand the growth temperature (Corti et al., 2010; Bakharev et al., 2014). Also noteworthy, the nanosprings' surface is terminated with free hydroxyl groups, which permits bonding with both organic and inorganic materials using common surface chemistry techniques (Schilke et al., 2010). Thus, proper functionalization will either promote, or prevent, wicking through the SN mats (Hass et al., 2012).

Additionally, two of the test surfaces were engineered with an underlying roughness pattern. Surface 7-8 contained uniformly spaced microchannels (i.e. 25µm wide, 100µm apart), while Surface 9-10 contained a surface tension gradient consisting of variably spaced microchannels to help facilitate the movement of water to preferred locations on the surface as shown in Fig. 2. These surfaces were prepared using a Minitech desktop micro-milling machine housed in our lab. Prior to the SN coating, the surfaces were cleaned in an ultrasonic bath to remove any contaminants remaining from the machining process and were rinsed in isopropyl alcohol, acetone, and finally deionized water.

2.2 Defrosting Experiments

A brief overview of the test setup and experimentation are discussed here, while a more detailed explanation can be found in Schmiesing and Sommers (2017). The defrosting experiments were conducted in a controlled environment chamber made of Plexiglas (see Fig. 3). During testing, the relative humidity within the chamber and the test surface temperature were capable of being controlled. The test surfaces (A) were attached to a thermoelectric cooler (TEC) (B) using four Nylon screws with Teflon spacers and thermal paste. Holes were machined approximately 6-8 mm deep in the side of each test plate to allow T-type thermocouples to measure the surface temperature and insulation was applied to the TEC to minimize unwanted heat loss. This surface-TEC setup was placed upon a GP5202 Satorius balance (C). With this arrangement, real-time frost mass measurements were recorded every 10 seconds, allowing for

the direct calculation of the defrost percentage. A drip tray (D) was positioned below the test surface to capture the drainage during defrost periods to prevent any interference with the mass balance. To limit the heat transfer effects of the warm air given off by the TEC, the test chamber was separated into two subsections with a divider (E) and an exhaust hole was machined into the chamber wall. The relative humidity and surrounding temperature were monitored with an OMEGA OM-73 data logger (F). The relative humidity was also monitored with a set-point controller (G) that toggled an ultrasonic cool mist humidifier ON and OFF, which provided humidified air through a tube (H).

Cyclical frost/defrost tests were conducted to assess the defrost performance of each surface. Each frost cycle contained a 1-hour frost period and a 30 minute defrost period. To fully evaluate each test surface at the prescribed conditions, three cycles were carried out resulting in each test lasting 3 hours and 30 minutes. The tests presented in this paper were all conducted at 60% relative humidity and one of three temperatures, -8℃, -10℃, or -12℃. Prior to the start of each test, a thin plastic layer was placed across the test surface to deter any premature frost growth. Then, the desired relative humidity was obtained using the cool mist humidifier while the surface temperature was controlled by adjusting the DC voltage source used to operate the TEC. Defrosting and frosting periods were initiated by toggling the TEC power supply OFF and ON respectively. During the defrost periods, the humidifier was also toggled OFF to prevent any interference with the defrosting results. With this test setup and procedure, the temperature could be held constant within ±0.5ºC and the relative humidity was maintained within ±2-3%. During testing, the ambient temperature varied between 21-23℃ and the difference in surface temperature was less than 1℃ between tests at the same conditions. To ensure the repeatability of our methodology, multiple tests were conducted under the same conditions. Figure 3b shows a representative test that highlights the repeatability of these experiments.

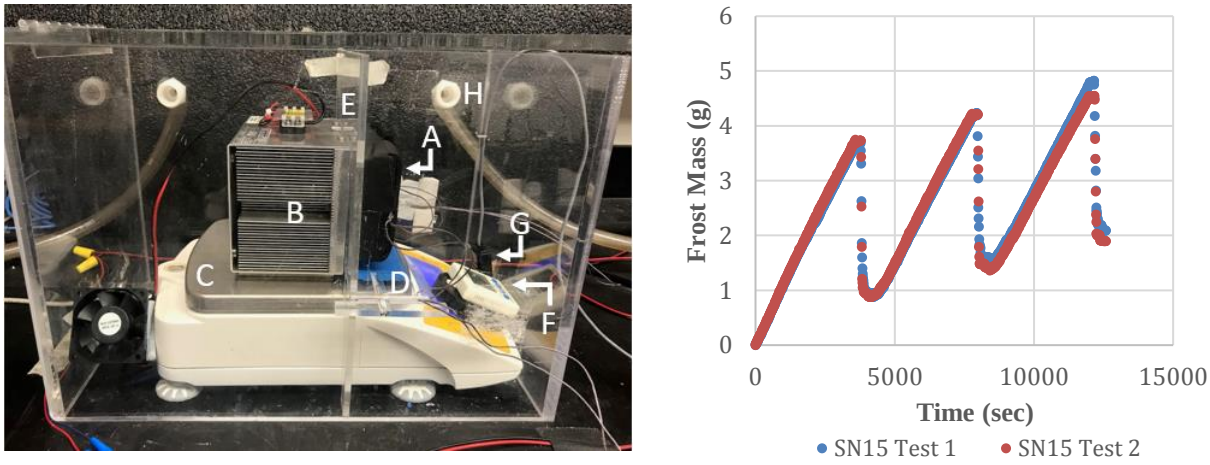

Figure 3: (a) Environmental chamber used for defrosting experiments. The various components are identified in the text above. (b) The overall repeatability of these experiments was also checked. Shown is a representative test.

3. RESULTS AND DISCUSSION

3.1 Contact Angle Measurements

In this work, a ramé-hart contact angle goniometer was used to measure the static and dynamic contact angles of water droplets injected on the test samples using the sessile drop method (see Table 2). As shown in the table, several of the samples possessed a static contact angle of more than 150° which classifies the surface as being "super-hydrophobic." A few observations can be made. First, silica nanospring coated surfaces, the static CA increased and the contact angle hysteresis (i.e. $\theta_{adv} - \theta_{rec}$) generally decreased as the coating thickness increased. For example, on Surface 5, the static CA was more than 165°, and the hysteresis was < 7°. (Note: Droplet mobility is typically enhanced on surfaces with low contact angle hysteresis.) In contrast, the baseline surface had the highest overall hysteresis (i.e. ~ 40°) among the homogeneous test surfaces. Second, for Surface 4 (i.e. SN Coating 3), the measured contact angles before and after

the defrost experiments were within 1° of each other. This suggests not only good repeatability for these measurements, but also a certain "robustness" to the SN coating. (i.e. Its overall effectiveness did not deteriorate with repeated frost-defrost testing. In contrast, some of the earlier SN coated surfaces (i.e. thicker coatings) showed evidence of performance deterioration with time.) Third and finally, the static CA on the coated gradient surface (i.e. S10) compared favorably with the static CA on Surface 5 which contained the same SN mat thickness. This suggests that the non-wetting behavior of the surface is more strongly influenced by the nanoscale characteristics (than either the microscale or macroscale), and that good repeatability can be achieved when growing nanosprings on a surface.

Table 2: Contact angles on test plates*

No.	Surface	Surface ID	Static CA	θ_{adv}	θ_{rec}	Hysteresis
S1	Baseline Surface	--	99.0°	110.4°	70.5°	39.9°
S2	Baseline + SN Coating Thickness 1	SN30	154.6°	161.4°	130.6°	30.8°
S3	Baseline + SN Coating Thickness 2	SN15	152.3°	161.6°	130.0°	31.6°
S4a	Baseline + SN Coating Thickness 3	SN5	164.7°	166.9°	156.7°	**10.2°**
S4b	Baseline + SN Coating Thickness 3†		165.0°	167.8°	156.0°	**11.8°**
S5	Baseline + SN Coating Thickness 4	SN2	**165.8°**	166.9°	160.0°	6.9°
S6	Baseline + SN Coating Thickness 5	SN1	*n/a*	*n/a*	*n/a*	--
S7	Uniform Channels (uncoated)	--	127.5°	157.3°	77.1°	80.2°
S8	Uniform Channels + SN Coating 4	--	*n/a*	*n/a*	*n/a*	--
S9	Gradient Surface (uncoated)‡	--	150.5°	157.3°	114.4°	42.9°
S10	Gradient Surface + SN Coating 4‡	--	**164.9°**	*n/a*	*n/a*	--

*Measured before experiments unless otherwise noted †After experiments ‡ Hydrophobic region (channels ‖ camera)

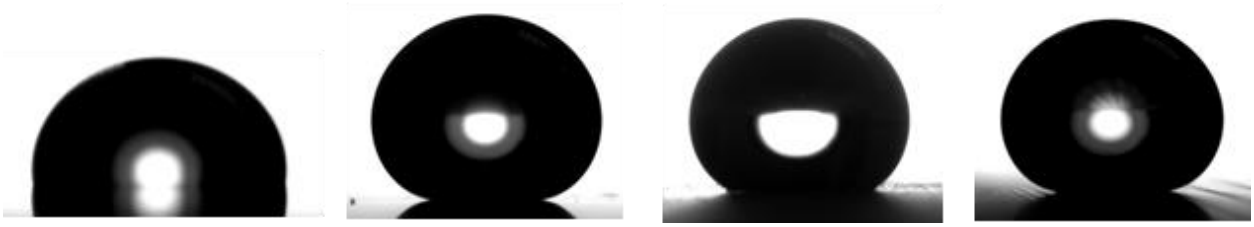

S1-baseline | S5-nanosprings 4 (SN2) | S9-gradient (uncoated) | S10-gradient (nanosprings coated)

Figure 4: Static contact angles on representative test surfaces

3.2 Silica Nanospring Surfaces

The results from the defrosting experiments are plotted below in Fig. 5. Shown is the defrosting percentage (%) of the surface over three cycles for the baseline surface and the five SN coated surfaces. In this table, the "defrosting percentage" is defined as the ratio of drained water mass to the initial frost mass on the surface prior to defrosting. The relative humidity was held constant at 60% for these experiments, and three different surface temperatures (i.e. -8°C, -10°C, and -12 °C) were examined. (Note: These represent typical surface temperature values. Small differences (< 1°C) were observed from test to test.) A few observations here are worth noting. First, the defrosting percentage generally increased with decreasing thickness of the SN mat. For example, SN30 consistently performed worse than SN15 and SN5. It is speculated that the thicker SN coatings are more susceptible to damage and breakage of the nanosprings from the surface due to the infiltration of water into the mat and subsequent freezing. Preliminary evidence suggests that the SN2 coating (or perhaps SN1) which represents a thinner coating may be more optimal for these frost/defrost experiments. This is further supported by the contact angle data in Table 2, which showed significantly higher CA hysteresis values for the SN30 and SN15 coated surfaces. Second, in all cases, SN5, SN2, and SN1 performed better than the baseline surface. This was observed at all three surface temperatures and across all

three defrost cycles. This is a strong indication that thin SN mats are fairly robust and can improve defrosting efficiency over conventional surfaces. Third, the defrosting percentage increased as the surface temperature decreased. In fact, the highest defrosting percentages (nearly 90%) were observed during the −12°C experiments. This is likely due to differences in the frost morphology and/or the initial frost mass on the surface. Because more frost mass tends to accumulate on colder surfaces, the likelihood for "droplet sweeping" (i.e. process by which a draining droplet will carry other droplets with it) may be increased during defrosting. Fourth and finally, the defrosting performance generally decreased with each cycle with the lowest defrosting percentage typically occurring in cycle 3. In most cases, the performance drop ranged from 7-15% over the three cycles. This highlights the need for multiple cycle experiments and suggests that the use of the 1st cycle defrosting percentage to predict future performance could lead to significant error.

3.3 Patterned Surfaces with SN Coating

After the tests were performed on the SN-coated baseline surfaces to determine a near optimal coating thickness, defrosting experiments were performed on two different micro-milled patterned surfaces (with and without the SN coating)— i.e. one containing uniformly-spaced microchannels and the other containing variably-spaced microchannels in order to create a wettability gradient. The data from these experiments are plotted in Fig. 6. A few things should be noted. First, in all cases as might be expected, the SN-coated version of the surface outperformed the uncoated version of the surface. In several cases, the percent enhancement was more than 10%. Second, in almost all cases, the SN-coated patterned surfaces (i.e. S8, S10) outperformed the baseline SN-coated surface (i.e. S5). It is believed that the directionality of the surface and the reduced contact area are the main contributing factors behind this improvement. It is thought that the surface at the bottom of the channel warms above the melting point before the

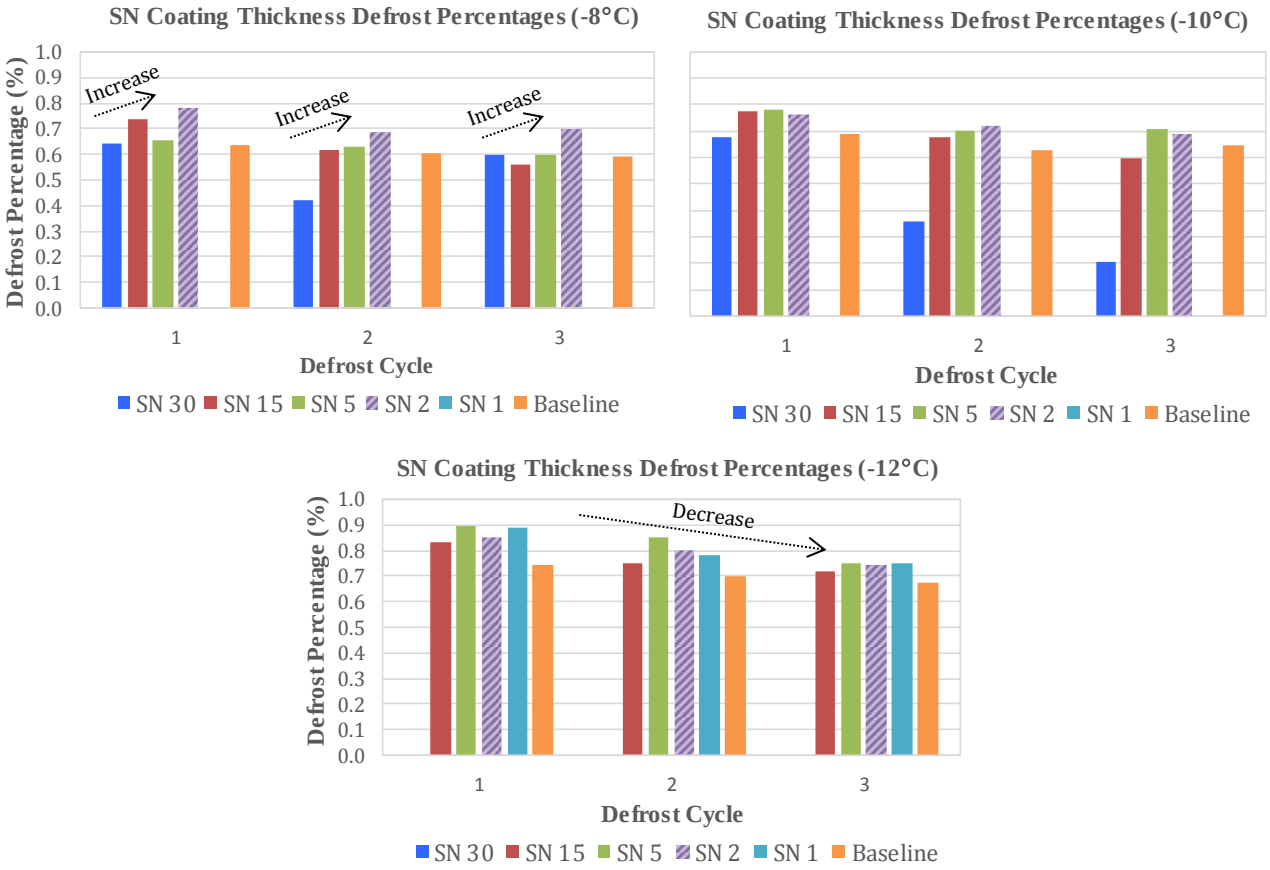

Figure 5: Defrosting efficiency (%) for the baseline SN-coated surfaces over three consecutive frosting/defrosting cycles for three different surface temperatures

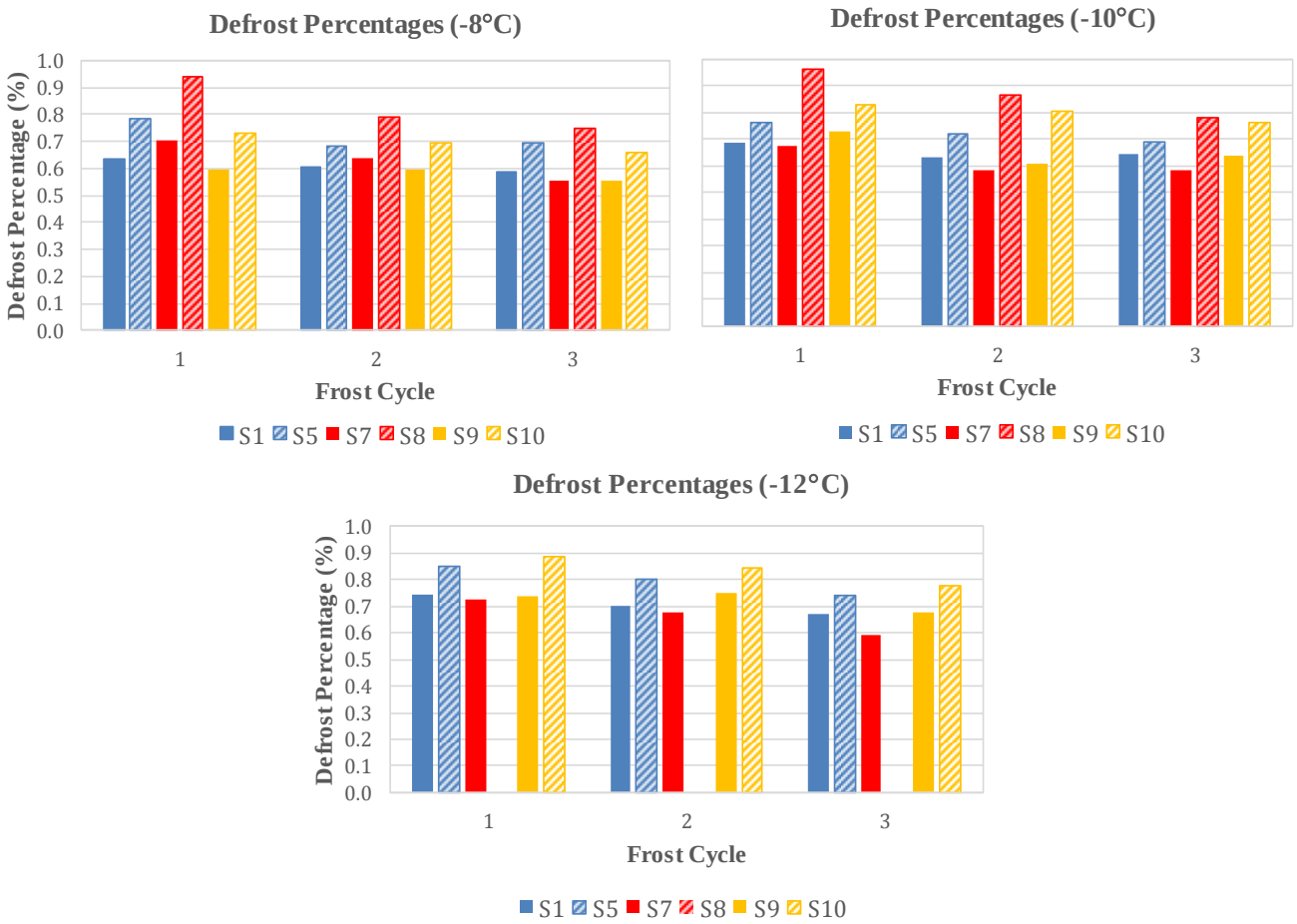

Figure 6: Defrosting performance of the patterned SN-coated surfaces over three defrost cycles for three temperatures (S1=baseline, S5=baseline + SN2 coating, S7=uniform channels, S8=uniform + SN2, S9=gradient, S10=gradient + SN2)

raised part. This leads to a thin layer of meltwater underneath the frost layer, which in turn can aid in its drainage and/or removal from the surface. Third, the SN-coated uniform channel surface (i.e. S8) clearly performed the best of the tested surfaces. In fact, in a couple of cases, the defrosting percentage associated with this surface exceeded 90% (i.e. specifically, 94% and 96%). Fourth, the SN-coated gradient surface (i.e. S10) appeared to perform better at –12°C versus –8°C (i.e. colder surface temperatures). While the reason for this difference is not known at this time, the difference was statistically significant and repeatable. Moreover, this dependency was observed previously for this gradient surface in earlier work (Schmiesing and Sommers, 2017). It is believed that this may stem from small differences in the frost layer density and the overall ice crystal structure at these temperatures. For example, it is well known that frost tends to be fluffier and less dense on colder surfaces (Hayashi, 1977). Thus, if the frost is fluffier at –12°C and more discrete droplets are formed during the melting process, this might better facilitate the coalescence of individual droplets and thus the usefulness of the underlying gradient pattern. At this time, however, the reason for this difference is not known.

4. CONCLUSIONS

In this work, the contact angles and defrosting performance of five different surfaces coated with a novel silica nanospring mat of varying thickness were measured. The measurements were made to determine how effective the coating was at repelling and draining water and what the "optimal" coating thickness might be. It was found that the thinner coatings performed better with some preliminary evidence suggesting that they might also be more robust. More specifically, the SN2 coating (grown for ~2 minutes) with a thickness of approximately 500 nm performed best.

After establishing the ideal SN coating thickness, two different microstructural surface patterns were then examined both before and after the growth of the silica nanospring coating on the surface (i.e. S7-S10). One of these surfaces

contained uniformly-spaced microchannels 25μm wide, 100μm apart (i.e. S7, S8), while the other contained a surface tension gradient consisting of variably spaced microchannels designed to help facilitate the movement of water to preferred locations on the surface (i.e. S9, S10). Defrost experiments were then performed on each of these surfaces and compared with the baseline surface (i.e. S1) and the baseline surface containing the SN2 coating (i.e. S5). Overall, the surface defrosting percentage varied from 56-96% depending on the surface and test conditions. The SN-coated surfaces however consistently outperformed the baseline surface with the highest recorded defrosting percentages occurring on the SN-coated uniformly spaced microchannel surface (i.e. S8) and the gradient surface (i.e. S10). The percentage improvement over the uncoated baseline surface was generally 10-16% although increases in defrosting percentage as high 23-30% were recorded.

At $T_w = -8°C$, the highest defrosting percentage (i.e. 94%) belonged to the SN-coated, uniformly spaced microchannel surface (i.e. S8), while the lowest defrosting percentage (i.e. 56%) belonged to the uncoated microchannel surface (i.e. S7). In contrast, at $T_w = -12°C$, the highest defrosting percentage (i.e. 89%) belonged to the SN-coated gradient surface (i.e. S10), while the lowest defrosting percentage (i.e. 59%) again belonged to the uncoated microchannel surface (i.e. S7). It should be pointed out, however, that the SN-coated microchannel surface (i.e. S8) was never tested at this lowest temperature condition. Our data also showed that the defrosting percentage generally decreased from cycle to cycle over the three frost/defrost cycles tested. The defrosting percentage was also somewhat higher on average when the frost layer was grown at lower surface temperatures (i.e. −12°C vs. −8°C) suggesting a possible link between defrosting effectiveness and the properties of the grown frost layer. Additional testing however is needed to substantiate this idea. Each experiment consisted of three distinct frost/defrost cycles which were each compromised of one hour of frost growth, followed by ten minutes of defrost and water drainage.

NOMENCLATURE

A	heat transfer area	(m^2)	**Greek Symbols**	
CA	contact angle	(°)	δ	thickness (nm or mm)
m	frost mass	(g)	θ	contact angle
RH	relative humidity	(%)	**Subscripts**	
t	time	(sec)	a	air
T	temperature	(°C)	w	wall surface

REFERENCES

Bakharev, P., Dobrokhotov, V., McIlroy, D. (2014). A method for integrating ZnO coated nanosprings into a low cost redox-based chemical sensor and catalytic tool for determining gas phase reaction kinetics, *Chemosensors*, 2, 56–68.

Cai, L., Wang, R., Hou, P., Zhang, X. (2011). Study on restraining frost growth at initial stage by hydrophobic coating and hygroscopic coating, *Energy and Buildings* 43, 1159-1163.

Cheng, C.-H., Cheng, Y.-C. (2001). Predictions of frost growth on a cold plate in atmospheric air, *Int. Comm. Heat Mass Transfer* 28(7), 953-962.

Corti, G., Wang, L., Major, D., Jabal, J., Branen, L., Nagler, J., Aston, E., Norton, G., McIlroy, D. (2007). Nanospring-Based Biosensors for Electrical DNA Microarrays, *Mater. Res. Soc. Symp. Proc.*, vol. 1010E, pp. V05–03.

Corti, G., Cantrell, T., Beaux II, M. F., McIlroy, D. N., Norton, G. (2010). Next Generation Nanospring- Enhanced Catalytic Converters, presented at the *Nanotech Conference & Expo 2010*, Anaheim, CA.

Corti, G., Yingqian Z., Lidong W., Brian H., Timothy C., Miles B. II, Tej P., F Marty Y., Michael A M., and David N M. (2013). The Effects of Nanoscale Geometry and Spillover on Room Temperature Storage of Hydrogen on Silica Nanosprings. *Journal of Physics D: Applied Physics* 46 (50), 505307.

El Cheikh, A. Jacobi, A. (2014). A mathematical model for frost growth and densification on flat surfaces, *Int. J. Heat Mass Transfer* 77, 604-611.

Fang, G., Amirfazli, A. (2014). Understanding the anti-icing behavior of superhydrophobic surfaces, *Surface Innovations* 2, 94-102.

Hass, J. L., Garrison, E. M., Wicher, S. A., Knapp, B., Bridges, N., Mcllroy, D., Arrizabalaga, G. (2012). Synthetic osteogenic extracellular matrix formed by coated silicon dioxide nanosprings, *J. Nanobiotechnology*, 10(1), 6.

Hayashi, Y., Auki, A., Adachi, S., Hori, K. (1977). Study of frost properties correlating with frost formation types, *J. Heat Transfer* 99, 239-245.

Hermes, C.J.L., Loyola, F.R., Nascimento Jr., V.S. (2014). A semi-empirical correlation for the frost density, *Int. J. Refrig.* 46, 100-104.

Hoke, J.L., Georgiadis, J.G., Jacobi, A.M. (2004). Effect of substrate wettability on frost properties, *J. Thermophysics and Heat Transfer* 18(2), 228-235.

Huang, L., Liu, Z., Liu, Y., Gou, Y., Wang, L. (2012). Effect of contact angle on water droplet freezing process on a cold flat surface, *Exp. Therm. Fluid Sci.* 40, 74-80.

Iragorry, J., Tao, Y.-X., and Jia, S. (2004). A Critical Review of Properties and Models for Frost Formation Analysis, *HVAC&R Research*, 10(4), 393-419.

Kandula, M. (2011). Correlation of water frost porosity in laminar flow over flat surfaces, *Special Top. Rev. Porous Media – Int. J.* 3, 79-87.

Kim, K., Lee, K.-S. (2011). Frosting and defrosting characteristics of a fin according to surface contact angle, *Int. J. Heat Mass Trans.* 54, 2758-2764.

Kim, K., Lee, K.-S. (2012). Characteristics and performance evaluation of surface-treated louvered-fin heat exchangers under frosting and wet conditions, *Int. J. Heat Mass Transfer* 55, 6676-6681.

Kim, K., Lee, K.-S. (2013). Frosting and defrosting characteristics of surface-treated louvered-fin heat exchangers: Effects of fin pitch and experimental conditions, *Int. J. Heat Mass Transfer* 60, 505-511.

Kim, M., Kim, H., Lee, K., Kim, D. (2017). Frosting characteristics on hydrophobic and superhydrophobic surfaces: A review, *Energ. Convers. Manage.* 138, 1-11.

Kulinich, S.A., Farhadi, S., Nose, K., Du, X.W. (2011). Superhydrophobic surfaces: Are they really ice-repellent? *Langmuir* 27(1), 25-29.

Lee, K.S., Kim, W.S., Lee, T.H. (1997). A one-dimensional model for frost formation on a cold flat surface, *Int. J. Heat Mass Transfer* 40(18), 4359-4365.

Liu, Y., Kulacki, F.A., (2018). An experimental study of defrost on treated surfaces: Effect of frost slumping, *Int. J. Heat Mass Transfer* 119, 880-890.

Liu, Z., Gou, Y., Wang, J., Cheng, S. (2008). Frost formation on a super-hydrophobic surface under natural convection conditions, *Int. J. Heat Mass Transfer* 51, 5975-5982.

McIlroy, D. N., Alkhateeb, A., Zhang, D., Aston, D. E., Marcy, A. C., Norton, M. G. (2004). Nanospring formation— unexpected catalyst mediated growth, *J. Phys. Condens. Matter*, 16(12), R415–R440.

O'Neal, D. L., and Tree, D. R. (1984). Measurement of Frost Growth and Density in a Parallel Plate Geometry, *ASHRAE Transactions*, 90(2A), 278–290.

Padki, M. M., Sherif, S. A., and Nelson, R. M. (1989). A Simple Method for Modeling the Frost Formation Phenomenon in Different Geometries, *ASHRAE Transactions*, 95(2), 1127–1137.

Rahimi, M., Afshari, A., Fojan, P., Gurevich, L. (2015). The effect of surface modification on initial ice formation on aluminum surfaces, *Applied Surface Science* 355, 327-333.

Sai, V. V. R., Gangadean, D., Niraula, I., Jabal, J. M. F., Corti, G., McIlroy, D. N., Aston, D. E., Branen, J. R., Hrdlicka, P. J. (2011). Silica Nanosprings Coated with Noble Metal Nanoparticles: Highly Active SERS Substrates, *J. Phys. Chem. C*, 115(2), 453–459.

Schilke, K. F., Wilson, K. L., Cantrell, T., Corti, G., McIlroy, D. N., Kelly, C. (2010). A novel enzymatic microreactor w/ Aspergillus oryzae β-galactosidase immobilized on silicon dioxide nanosprings, *Biotechnol. Prog.*, 26, 1597–1605.

Schmiesing, N.C., Sommers, A.D. (2017). Defrosting performance on hydrophilic, hydrophobic, and micro-patterned gradient heat transfer surfaces, *Science and Technology for the Built Environment* 23, 946-959.

Shin, J., Tikhonov, A.V., Kim, C. (2003). Experimental study on frost structure on surfaces with different hydrophilicity: density and thermal conductivity, *J. Heat Transfer* 125, 84-94.

Song, M., Dang, C. (2018). Review on the measurement and calculation of frost characteristics, *Int. J. Heat Mass Transfer* 124, 586-614.

Tao, Y.X., Besant, R.W., Rezkallah, K.S. (1993). A mathematical model for predicting the densification and growth of frost on a flat plate, *Int. J. Heat Mass Transfer* 36(2), 353-363.

Timalsina, Y. P., Oriero, D., Cantrell, T., Prakash, T., Branen, J., Aston, D. E., Noren, K., Nagler, J. J., Rastogi, S., McIlroy, D. N., Corti, G. (2010). Characterization of a vertically aligned silica nanospringbased sensor by alternating current impedance spectroscopy, *J. Micromechanics Microengineering*, 20(9), 095005.

Tokura, I., Saito, H., Kishinami, K. (1983). Study on properties and growth rate of frost layers on cold surfaces, *J. Heat Transfer* 105(4), 895-901.

Tourkine, P., Le Merrer, M., Quéré, D. (2009). Delayed freezing on water repellent materials, *Langmuir* 25, 7214-16.

Wang, L., Major, D., Paga, P., Zhang, D., Norton, M. G., McIlroy, D. N. (2006). High yield synthesis and lithography of silica-based nanospring mats, *Nanotechnology*, 17(11), S298–S303.

Wang, Z.-J., Kwon, D.-J., DeVries, K.L., Park, J.-M. (2015). Frost formation and anti-icing performance of a hydrophobic coating on aluminum, *Exp. Therm. Fluid Sci.* 60, 132-137.

Yang, D.K., Lee, K.S. (2004). Dimensionless correlations of frost properties on a cold plate, *Int. J. Refrig.* 27, 89-96.

Yonko, J.D., Sepsy, S.F. (1967). An investigation of the thermal conductivity of frost while forming on a flat horizontal plate, *ASHRAE Transactions* 73(2), 1.1-1.11.

Yun, R., Kim, Y., and M. Min (2002). Modeling of frost growth and frost properties with airflow over a flat plate, *Int. J. Refrig.* 25(3), 362-371.